

Numerical Simulation of Subsonic and Supersonic Impinging Jets

Robert Wilke and Jörn Sesterhenn

Abstract This report concentrates on fully turbulent confined round impinging jets with focus on heat transfer and the source mechanism of the impinging tones. Direct numerical simulations were performed with Reynolds numbers of $Re = 3300$ (subsonic and supersonic) and $Re = 8000$ (subsonic) using grid sizes of $512 \times 512 \times 512$ respectively $1024 \times 1024 \times 1024$ points. The transient flow field is analysed using a dynamic mode decomposition (DMD). It is shown that there is a dominant frequency with which the heat transfer at the impinging plate fluctuates. The corresponding structures are the vortex rings developing in the shear layer of the free jet region of the impinging jet. The same structures are together with the standoff shock responsible for the discrete tones referred to as impinging tones emitted by supersonic impinging jets.

1 Introduction

Subsonic impinging jets provide an effective cooling method for various applications such as the cooling of turbine blades of aircraft. No less important is the usage as rocket engine or vertical and/or short take-off and landing (V/STOL) aircraft aero engine. Those jets are typically operated under pressure ratios high enough to allow a supersonic flow. The operation is characterised by the emission of destructive loud noise that can cause material fatigue and deafness.

Both, heat transfer and jet noise are investigated using direct numerical simulations (DNS). Each project is described in an own section (Sects. 3 and 4) after the common numerical framework is explained (Sect. 2).

R. Wilke (✉) • J. Sesterhenn

Technische Universität Berlin, Fachgebiet Numerische Fluidodynamik, Müller-Breslau-Str. 11, 10623 Berlin, Germany

e-mail: robert.wilke@tnt.tu-berlin.de; joern.sesterhenn@tu-berlin.de; <http://www.cfd.tu-berlin.de/>

2 Numerical Method

2.1 Discretisation

The governing Navier-Stokes equations are formulated in a characteristic pressure-velocity-entropy-formulation, as described by Sesterhenn [25] and solved directly numerically. This formulation has advantages in the fields of boundary conditions, parallelization and space discretisation. No turbulence modelling is required since the smallest scales of turbulent motion are resolved. The spatial discretisation uses 6th order compact central schemes of Lele [16] for the diffusive terms and compact 5th order upwind finite differences of Adams et al. [1] for the convective terms. To advance in time a 4th order Runge-Kutta scheme is applied. In order to avoid Gibbs oscillations in the vicinity of the standoff shock (present at supersonic impinging jets) an adaptive shock-capturing filter developed by Bogey et al. [2] that automatically detects shocks is used.

2.2 Computation of Statistical Variables

The impinging jet at $Re = 8000$ has to be resolved with more than one billion grid points in order to achieve an adequate spacial resolution of the Kolmogorov scales. Storing one time step with the necessary five variables (pressure, velocity (x,y,z) and entropy) requires 41 GB of storage. It is easily noticeable that it is not sensible today to store thousands of time steps so as to do statistical analysis as post-processing. Therefore the code was restructured in 2014 and allows now the computation of statistical variables e.g. mean values, variances or complicated budget terms on-the-fly. This is done in four steps. In the first step the simulation runs until the influence of the start e.g. the starting of the impinging jet is faded away and the flow reaches a settled or periodic state. Afterwards, mean values of the required variables and terms are computed. In the third step, fluctuations of expressions are computed. In the final step only operation on mean values obtained in the second and third step are performed. Applying this strategy, the required storage is reduced to a fraction, but one has to be very carefully since additional quantities may not be computable after the simulation was conducted.

2.3 High Performance Computing

Investigating physics by means of direct numerical simulation requires huge computing capacity, which can only be provided by the most powerful high performance computers that are available nowadays. The Kolomgorov scales that need to be resolved lead at high Reynolds numbers of $Re = 8000$ to capacities in the order

of much more than ten million core hours per computation. The load is partitioned between a huge number of processes, e.g. 8192 or 16,384. Each process solves the Navier-Stokes equations for a fractional part of the computational domain (block). This approach is referred to as domain decomposition, see [7]. In order to calculate derivatives, information from the adjacent blocks are needed. Therefore the decomposed domain is rearranged so that each process receives grid lines that span the entire domain in the particular direction. The total number of grid points per process remains constant and is typically either 32^3 or 64^3 . Figure 1 exemplary shows the transformation from the original decomposition to the decomposition used for the calculation of derivatives in x-direction. The required inter-process communication is managed via MPI libraries.

The code has been successfully ported from CRAY XE6 (Hermit) to CRAY XC40 (Hornet). Figure 2 shows nearly perfect linear scaling up to 16,384 cores

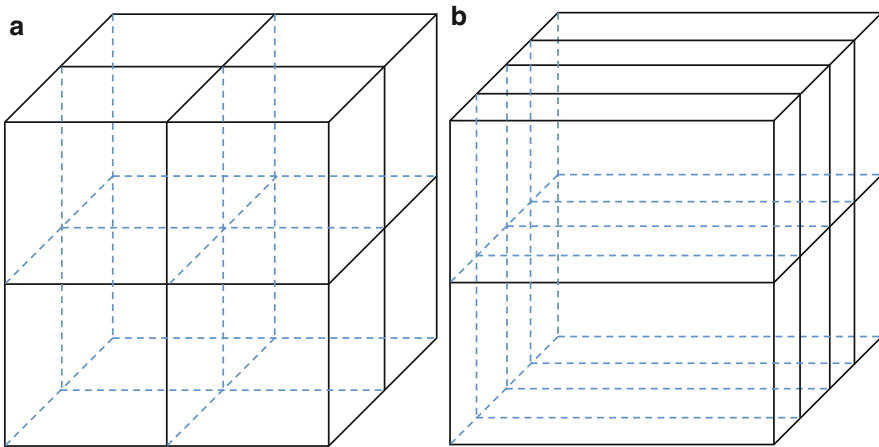


Fig. 1 Domain decomposition of a three-dimensional domain. (a) Original decomposition; (b) Transformed decomposition for the calculation of derivatives in x-direction

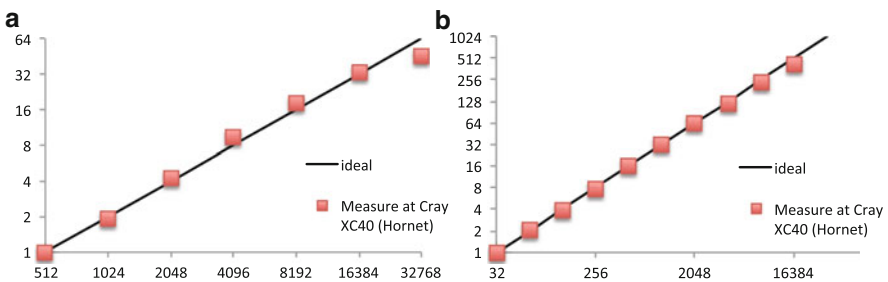


Fig. 2 Strong and weak scaling of the code on CRAY XC40 (Hornet) (a) Strong scaling; simulations run with 1024^3 grid points; (b) Weak scaling; simulations run with 64^3 grid points per core

for the given problem. Using auto-vectorisation, the efficiency with 16,384 cores is 102 % (strong) respectively 83 % (weak) enables to efficiently perform computations on Hornet with 16,384 cores. Grids with 512^3 (1024^3) points are typically parallelized on $16^3 = 4096$ ($32 \times 16 \times 16 = 8192$ or $32 \times 32 \times 16 = 16,384$) cores. The preferred wall time interval is 24 h.

2.4 Computational Domain

The present simulation is conducted on a numerical grid of size $512 \times 512 \times 512$ ($Re = 3300$) respectively $1024 \times 1024 \times 1024$ ($Re = 8000$) points for the computational domain sized $12D \times 5D \times 12D$, where D is the inlet diameter, see Fig. 3. A confined impinging jet is characterised by the presence of two walls, the impinging plate and the orifice plate. The grid is refined in those wall-adjacent regions in order to ascertain a maximum value in time and space of the dimensionless wall distance y^+ of the closest grid point to the wall smaller than one for both plates. For the x - and z -direction a slight symmetric grid stretching is applied which refines the shear layer of the jet. The refinements use hyperbolic tangent respectively hyperbolic sin functions resulting in a change of the mesh spacing lower than 1 % for all directions and cases. Table 1 shows the physical parameters of the simulation.

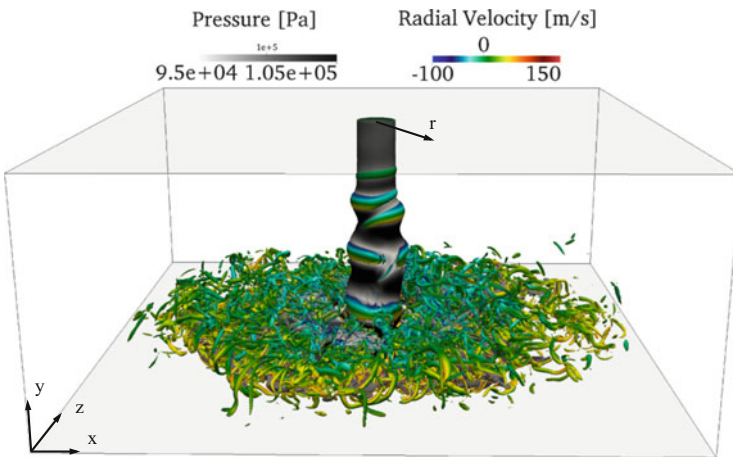


Fig. 3 Computational domain with iso-surfaces at $Ma = 0.2$ coloured with pressure and at $Q = 10^5 \text{ m}^2 \text{ s}^{-4}$ coloured with radial velocity. $Re = 8000$; $p_o/p_\infty = 1.5$

Table 1 Physical parameters of the simulation

p_o/p_∞	p_∞ (Pa)	Ma	T_o (K)	T_w (K)	Re	Pr	κ	R [J/(kg K)]
1.5	10^5	0.784	293.15	373.15	3300	0.71	1.4	287
1.5	10^5	0.784	293.15	373.15	8000	0.71	1.4	287
2.15	10^5	1.106	293.15	373.15	3300	0.71	1.4	287

$p_o, p_\infty, T_o, T_w, Re, Pr, \kappa, R$ denote the total pressure, ambient pressure, total temperature, wall temperature, Reynolds number, Prandtl number, ratio of specific heats and the specific gas constant

2.5 Boundary Conditions

The computational domain is delimited by four non-reflecting boundary conditions, one isothermal wall which is the impinging plate and one boundary consisting of an isothermal wall and the inlet. The walls are fully acoustically reflective. The location of the nozzle is defined using a hyperbolic tangent profile with a disturbed thin laminar annular shear layer as described in [31].

A sponge region is applied for the outlet area $r/D > 5$, that smoothly forces the values of pressure, velocity and entropy to reference values. This destroys vortices before leaving the computational domain. The reference values at the outlet were obtained by a preliminary large eddy simulation of a greater domain.

2.6 Kolmogorov Scales

The scales of turbulent motion span a huge range from the size of the domain to the smallest energy dissipating ones. Since the turbulent kinetic energy is transferred downwards to smaller and smaller scales, the smallest ones have to be resolved by the numerical grid in order to obtain a reliable solution of the turbulent flow. They are given with the kinematic viscosity ν and dissipation rate ϵ by $l_\eta \approx \left(\frac{\nu^3}{\epsilon}\right)^{\frac{1}{4}}$ and are valid for isotropic turbulence, that occurs at sufficiently high Reynolds numbers. The Reynolds numbers of 3300 and 8000 can be considered as low in that context or *not sufficiently high* to obtain isotropic turbulence. Therefore the Kolmogorov microscales provide a conservative clue.

The ratio of the mesh width to the Kolmogorov length scale $r_K = (h_x h_y h_z)^{1/3} / l_\eta$ reaches a maximum value of 1.6 ($Re = 3300$, subsonic) respectively 2.1 ($Re = 3300$, supersonic) at the lower wall. For supersonic turbulent boundary layers, Pirozzoli et al. [18] showed that the typical size of small-scale eddies is about $5..6l_\eta$. A strongly different behaviour for a boundary layer of high subsonic Mach number is not expected. The maximum ratio in the area of the free jet is $r_K = 1.3$ ($Re = 3300$, subsonic) respectively $r_K = 1.5$ ($Re = 3300$, supersonic) and of the

wall jet is $r_K = 1.5$ ($Re = 3300$, subsonic)/ $r_K = 1.5$ ($Re = 3300$, supersonic). At the standoff shock a value of $r_K = 2.7$ occurs and marks the global maximum.

2.7 Boundary Layer

In addition to the criterion due to turbulent motion of the jet, the boundary layer including the viscous sub-layer also has to be resolved appropriately in order to achieve reliable results of the heat transfer at the impinging plate. The maximum dimensionless wall distance y^+ of the present simulations $Re = 3300$ and ($Re = 8000$) occurs at $r/D = 0.46$ and reaches a value of $y^+ = 0.64$ ($y^+ = 0.58$). The minimum number of points in the viscous sub-layer $y^+ \leq 5$ is seven (eight) for the entire domain. Figure 4 shows the velocity- and temperature boundary layer profile for different distances from the stagnation point. u^+ and T^+ are the dimensionless radial velocity and the dimensionless temperature.

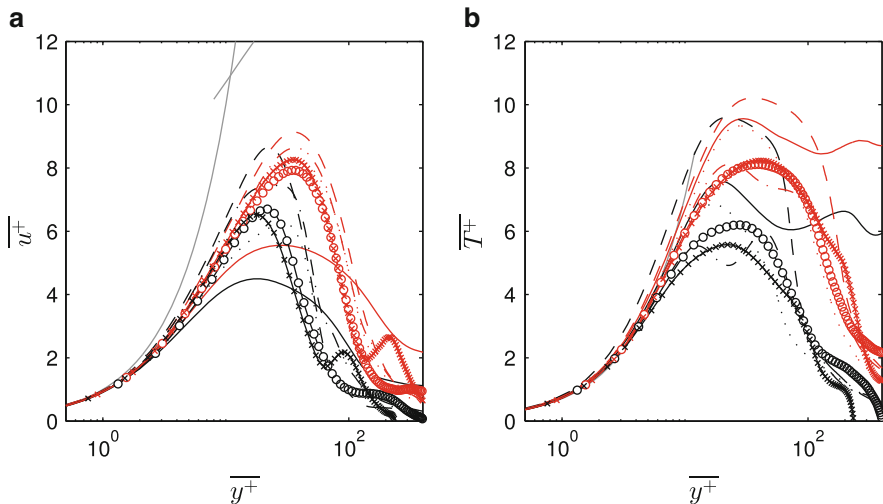


Fig. 4 Mean boundary layer profiles for different radial positions. *Black*: $Re = 3300$; *red*: $Re = 8000$. *Thick line*: $r/D = 0.5$, *Dashed line*: $r/D = 1.0$; *Dotted line*: $r/D = 1.5$; *Dashdotted line*: $r/D = 2.0$; *line with circles*: $r/D = 3.0$; *line with asterisks*: $r/D = 4.5$; *Thin line*: $u^+ = y^+$, $u^+ = \ln(y^+)/0.41 + 5.1$ respectively $T^+ = Pr y^+$. **(a)** Dimensionless Velocity; **(b)** Dimensionless Temperature

2.8 *Dynamic Mode Decomposition*

A dynamic mode decomposition (DMD) is used to relate coherent structures to the heat transfer characteristics of subsonic impinging jets (Sect. 3) and to tonal noise of the supersonic impinging jets (Sect. 4). The Dynamic Mode Decomposition (DMD) as described by Schmid and Sesterhenn [21–23] extracts dynamic information out of a sequence of snapshots for a specific time interval that are either generated experimentally or numerically. The temporal dynamics of the flow is approximated by a linear snapshot to snapshot operator. The dominant eigenfunctions of this evolution operator (companion matrix) form a set of dynamically relevant modal structures. The so called dynamic modes accurately describe the motion of the fluid and can be interpreted as a generalisation of global stability modes. The mathematical background as well as the algorithm are given in [21, 22].

3 Subsonic Jet Impingement Heat Transfer

3.1 *Introduction*

Impinging jets and have been studied for decades. General information including schematic illustrations of the flow fields as well as distributions of local Nusselt numbers for plenty of different geometrical configurations and Reynolds numbers Re can be found in several reviews, such as [12, 13, 29, 30] based on experimental and numerical results. Since experiments cannot provide all quantities of the entire flow domain spacially and temporally well resolved, the understanding of the turbulent flow field requires simulations. Most existing publications of numerical nature use either turbulence modelling for the closure of the Reynolds-averaged Navier-Stokes (RANS) equations, e.g. [33], or large eddy simulation (LES), e.g. [5]. Almost all available direct numerical simulations (DNS) are either two-dimensional, e.g. [4], or do not exhibit an appropriate spatial resolution in the three-dimensional case, e.g. [8]. Recent investigations come from Dairay et al. [6]. He conducted a DNS of a round impinging jet with a nozzle to plate distance of $h/D = 2$ and focused on the secondary maximum of the heat transfer distribution and the connection to elongated structures.

This study deals with direct numerical simulations of a turbulent round impinging jets with $h/D = 5$ and Reynolds numbers of $Re = 3300$ and $Re = 8000$. Both impinging jets are fully turbulent since the critical Reynolds number of the case is 3000 [12].

3.2 Results

3.2.1 Influence of The Reynolds Number

The results out of the strategy described in Sect. 2 are already available for the simulation at $Re = 3300$. The third step of the greater simulation is not completely converged at this time. In this section, we present some results of the first and second phase. Figure 5 shows mean distributions of the radial velocity and the temperature for different radial positions. As expected, both simulations have a similar mean flow field with the distinction, that the boundary layer thickness decreases with an increasing Reynolds number.

The mean Nusselt number

$$Nu(r) = -\frac{D}{\Delta T} \frac{\partial T}{\partial y}(r) \Big|_w \tag{1}$$

is shown in Fig. 6a and scaled with $Re^{0.555}$ Fig. 6b. The scaling law was linear interpolated from the laws for $h/D = 4$ and $h/D = 6$ found by Lee [15]. There are plenty of those laws determined from experiments. All of them are similar but the coefficients differ based on the set-up (nozzle shape, nozzle-to-plate distance,..). Regarding the scaled distributions, the Nusselt number profile of the simulations at $Re = 3300$ and ($Re = 8000$) feature a local maximum which is at once global, close to the axis of the jet at $r/D = 0.18$ ($r/D = 0.23$). The secondary maximum of the $Re = 3300$ case is located at $r/D = 1.1$. The $Re = 8000$ case does not have this secondary maximum, but it is visible that the slope in this area is decreased.

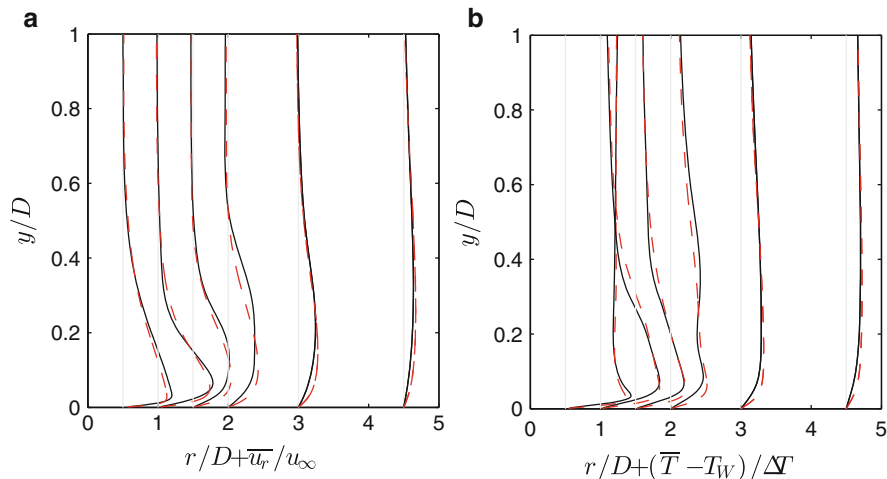


Fig. 5 Mean distributions for different radial positions r/D solid line: $Re = 3300$, red dashed line: $Re = 8000$. (a) Radial velocity; (b) Temperature difference $T - T_o$ relative to $\Delta T = T_w - T_o$

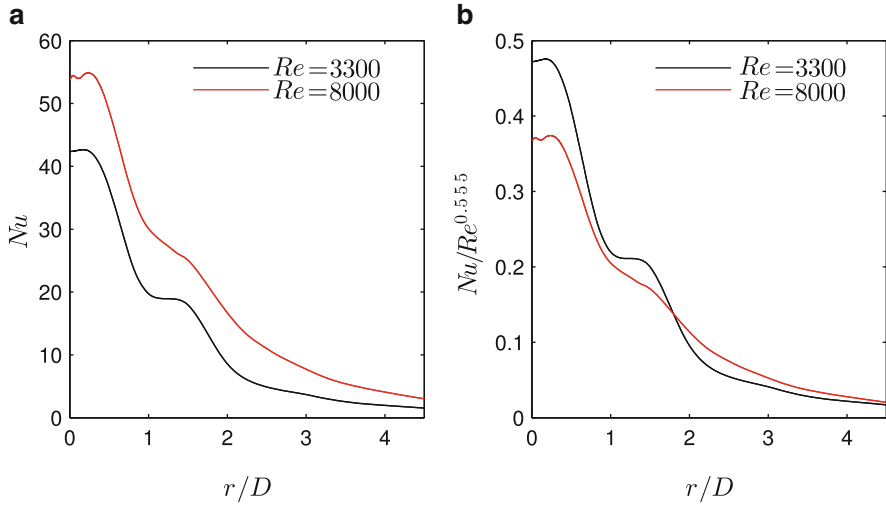


Fig. 6 Mean Nusselt number. (a) Mean Nusselt number; (b) Mean Nusselt number scaled with $Re^{0.555}$

A detailed analysis of the origins of this differences can and will be performed when all statistical results are available. However, the two maxima are connected to the primary vortex rings impinging on the plate close to the jet axis (primary maximum) respectively to a vortex pair (secondary maximum) consisting of the primary and a counter-rotating secondary vortex that moves from the stagnation point in radial direction until it breaks down into smaller structures [32]. Buchlin[3] reported for experimental data at much higher Reynolds numbers that $Re = 60000$ that the strength of both maxima decrease and the inner one moves to the stagnation point with increased nozzle to plate distances h/D and decreased Reynolds number. The simulation results show a reversed trend for the considered Reynolds numbers (Fig. 6).

3.2.2 The Dynamic Modes of Jet Impingement Heat Transfer

The aim of the performed DMD in this project is to find the modes corresponding to heat transfer characteristics of the impinging jet. Therefore a time series of the Nusselt number ($Re = 3300$) at the impinging plate is analysed beforehand of the DMD. The region $r/D = 1.2$ was chosen since it is located in the secondary maximum of the Nusselt number as illustrated in Fig. 6. The time series of an arbitrary point on the circle is shown in Fig. 7. The periodical behaviour of the Nusselt number is obvious. In order to determine the appropriate frequency range to be resolved with the DMD, a Fourier transformation of the time series around the circle $r/D = 1.2$ was conducted and then averaged. Figure 8 shows the spectrum of the signal whose amplitude A is measured in decibel with a reference value of

Fig. 7 Time series of the Nusselt number on an arbitrary point at $r/D = 1.2$, $Re = 3300$

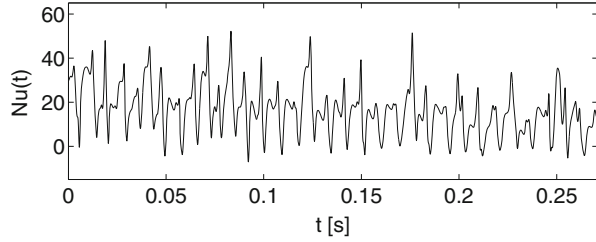
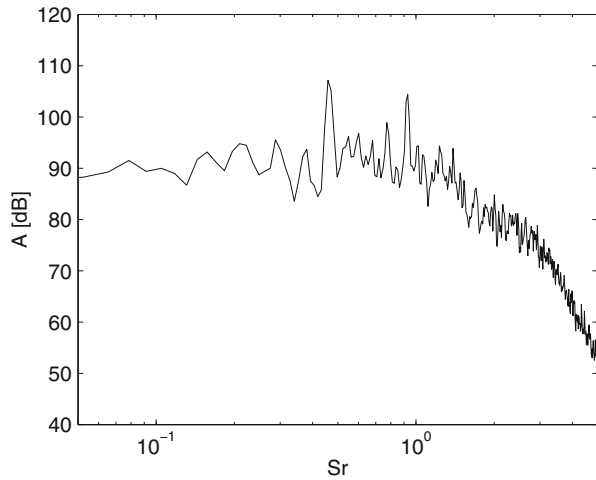


Fig. 8 Circumferential averaged FFT of the time series of the Nusselt number at $r/D = 1.2$, $Re = 3300$



2×10^{-5} . The spectrum exhibits two peaks with a Strouhal number of $Sr = 0.46$ and $Sr = 0.92$ corresponding to the first harmonic. Considering the dominant frequencies, a time span of 0.271 s represented by 120 snapshots and one out of four grid points ($128 \times 128 \times 128$) was used for the DMD.

Figure 9 shows the eigenvalue spectrum of the DMD. The imaginary part of the eigenvalues λ_i is equal to the dimensionless frequency of the dynamic structure whereas the real part quantifies the damping ($Re(\lambda_i) < 0$) or growing ($Re(\lambda_i) > 0$) of the mode. The mode at (0,0) represents the mean flow field since it has no frequency and is not damped. Pairs of complex conjugate eigenvectors and eigenvalues belong together to a single dynamic mode. The identified relevant frequencies of the time series of the Nusselt number $Sr = 0.46$ and $Sr = 0.92$ are marked additionally to the (0,0) eigenvalue in the figure.

The corresponding structures are illustrated in Fig. 10. The first column shows the Nusselt number at the impinging plate and Q (second invariant of the velocity gradient tensor) representing vortical structures on a cut through the jet axis. In the second column iso-surfaces of Q are snapped. The impinging plate represents the Nusselt Number again. The first row corresponds to the frequency $Sr = 0.46$ whereas the second one corresponds to $Sr = 0.92$. The superposition of both modes is shown in the third row. The DMD results show that the vortex rings developing in

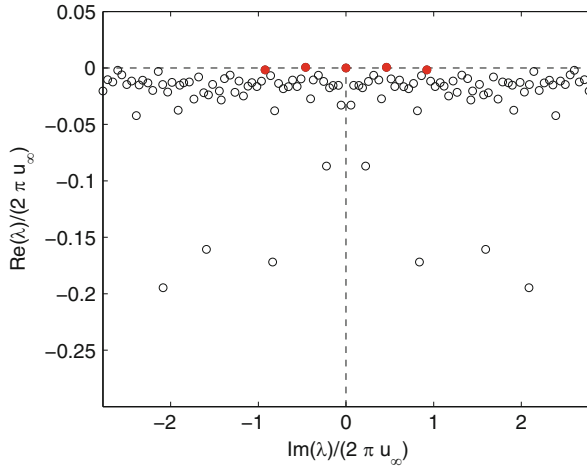


Fig. 9 Eigenvalue spectrum of the DMD, $Re = 3300$, marked frequencies: $0, \pm 0.46$ and ± 0.92

the shear layer are a superposition of a larger and a smaller structure. The larger structure corresponds to the frequency $St = 0.46$ and is the dominant one in the shear layer of the free jet region. The smaller one oscillates with the double frequency $St = 0.92$ and becomes important in the wall jet region. Both modes are axis-symmetric.

The DMD results are in agreement with the previously described relation between the movement of the vortical structures of the impinging jet and the dynamics of the Nusselt number on the impinging plate. The DMD delivers the dominant frequencies that are connected to the structures. This is an important step for heat transfer enhancement. Janetzke [14] showed that a pulsating inlet condition leads to an increase in heat transfer efficiency of more than 30% for Strouhal numbers in the range around $St = 0.9$. The reason behind the existence of this efficient frequency range remained unclear. Following the DMD results, it can be supposed that a pulsating inlet with the eigenfrequency of the impinging jet leads to an increase of the heat transfer efficiency. This theory will be verified in future work.

3.3 Conclusion

This report presents a dynamic mode decomposition (DMD) of data obtained from a direct numerical simulation of a subsonic confined impinging jet at $Re = 3300$. The spectral analysis of the time series of Nusselt number at the impinging plate features two dominant frequencies at $St = 0.46$ and $St = 0.92$. The same frequencies were found in the eigenvalue spectrum of the DMD. The corresponding structures match the primary and secondary vortex rings of the transient flow field of the impinging

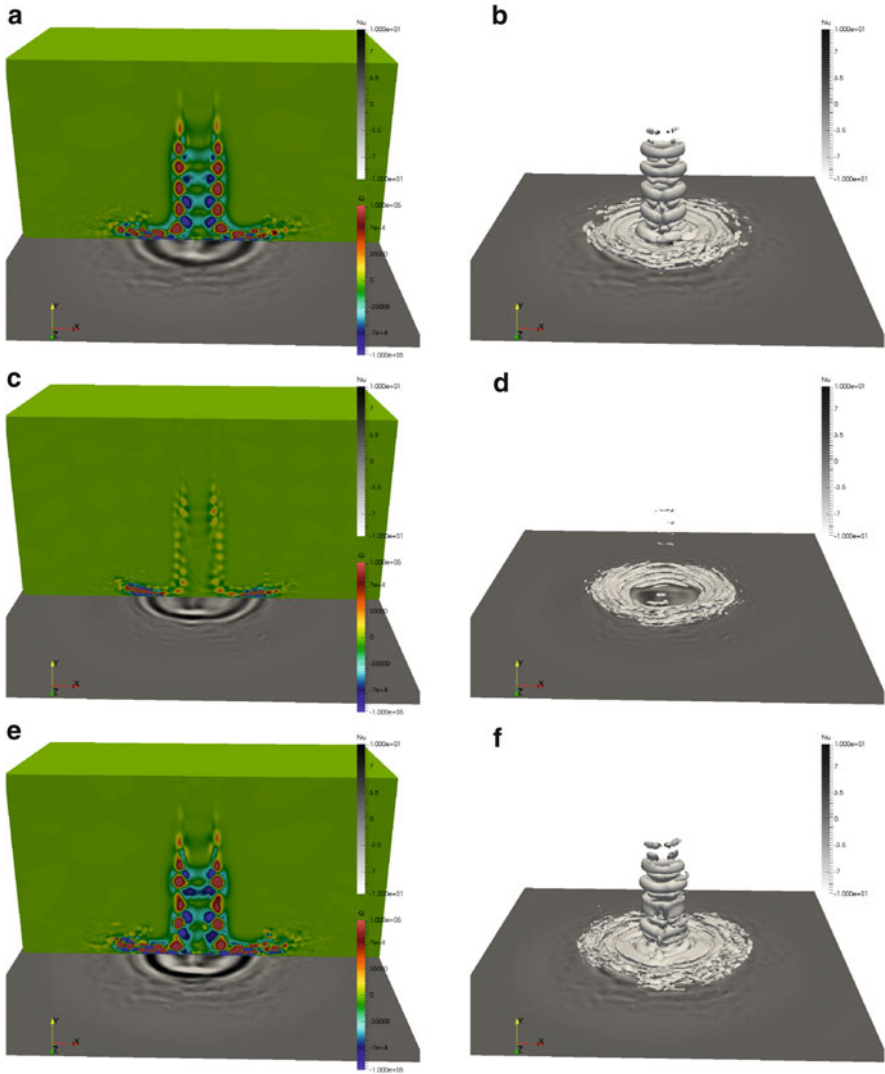


Fig. 10 Dynamic modes representing the periodical heat transfer characteristics of the impinging jet. The impinging plate is coloured with the Nusselt number. *First column:* Q (second invariant of the velocity gradient tensor) on a cut through the jet axis. *Second column:* iso-surfaces of Q . (a) $Sr = 0.46$; (b) $Sr = 0.46$; (c) $Sr = 0.92$; (d) $Sr = 0.92$; (e) $Sr = 0.46$ and $Sr = 0.92$; (f) $Sr = 0.46$ and $Sr = 0.92$

jet. Given the connection between the dominant frequencies and the unsteady heat transfer at the impinging plate, it can be supposed that a pulsating inlet with these dominant frequencies leads to an increase of the heat transfer efficiency of jet impingement.

4 Supersonic Impinging Jet Noise

4.1 Introduction

Compressible impinging jets are characterised by the appearance of immensely loud tonal noise. This noise can cause deafness and material fatigue. Until now the source mechanism is not completely understood. The discrete tones are an additional noise source to the ones occurring in the free jet.

In order to distinguish the impinging tones, a brief summary of the free jet noise sources following Tam [27] and Schulze [24] is given. For subsonic jets the only source is the turbulent mixing noise that is caused by large and small turbulent structures in the mixing layer of the jet. As soon as the nozzle pressure ratio (NPR) reaches a value to allow a supersonic flow, broadband shock-associated noise and screech noise appear as well in the case of under-expanded jets. Broadband shock-associated noise is caused by the interaction between downstream propagating large scale structures and the quasi periodic shock cell structure of the under-expanded jet.

Screech noise is a mark for discrete tones that are generated by a feedback mechanism. This source has to be distinguished carefully from the impinging tones, since both emit very strong tonal noise at similar frequencies. The screech noise feedback mechanism is shown in Fig. 11a. Vortical structures develop in the shear layer and grow while they are convected downstream. When the structures reach the fourth or fifth shock cell, they interact with those and emit strong acoustic waves that propagate upstream. These reach the nozzle lip or upper plate and excite the shear layer of the jet which leads to new instability waves and the close of the feedback mechanism. Based on the work of Powell [20] and Panda [17] five acoustic modes, labelled A-E, exist. They occur associated with the screech noise and therefore are

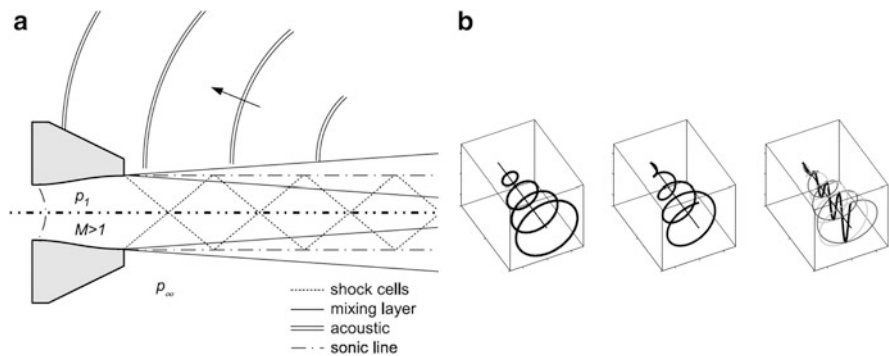


Fig. 11 The screech feedback loop and its associated acoustic modes of the free jet. (a) The screech feedback loop. Taken from [24]; (b) Instability modes of the free jet. *Left*: toroidal (axis symmetric), *middle*: helical, *right*: flapping (superposition of two counter-rotating helical modes). Adapted from [24]

referred to as screech modes. Depending on the nozzle pressure ratio, the free jet can feature varicose (toroidal) modes: A (A1, A2), helical modes: C or flapping modes that are a superposition of two counter-rotating helical modes: B, D. The shape of mode E is unknown. The mode shapes are sketched in Fig. 11b.

Supersonic impinging jet noise has been experimentally investigated for decades. However the source mechanism of the impinging tones is still not completely understood. First of all one has to distinguish between screech and impinging tones. Since the screech noise source is located between the rear edge of the third and the fifth shock cell, the distance between the nozzle/upper plate and the impinging plate has to be at least five diameters ($h/D \geq 5$) in order to allow the generation of screech tones [26]. Therefore a large proportion of the research was concentrated on very close plates and high pressure ratios ($NPR > 3$) [26]. It is generally agreed that a feedback mechanisms similar to the screech feedback loop is responsible for the appearance of impinging tones [9–11, 19]. However competing theories exist with respect to the close of the loop. Ho and Nosseir [11] named the primary vortices impinging on the wall as a possible link in the feedback chain. On the contrary Powell [19] and Henderson [10] suggested that standoff shock oscillations can have an important role in the feedback mechanism. A recent numerical investigation was performed by Uzun et al. [28]. He conducted a large eddy simulation with a plate distance of five diameters and a Mach number of 1.5 and found using a DMD coherent axis symmetric structures corresponding to the dominant tone at $Sr \approx 0.33$. A delimitation to screech and the missing mechanism in the feedback loop is not given.

In the present investigation a direct numerical simulation at $Re = 3300$, $NPR = 2.15$, $h/D = 5$ is carried out in order to identify the missing chain link in the impinging tone feedback mechanism by means of a dynamic mode decomposition (DMD). A delimitation to screech is given.

4.2 Results

4.2.1 Characterisation of the Discrete Tones of the Supersonic Impinging Jet: Distinction to Screech

The aim of this section is to show that the discrete tones occurring in the noise spectrum of the supersonic impinging jet are not related to screech. As explained, having a plate distance large enough, so that the relevant shock cells (number three to five) fit into the domain, it is possible that screech noise is radiated by the impinging jet. Figure 12 shows the pressure and axial velocity profile along the jet axis of the impinging jet. The profile is compared to one obtained from a free jet simulation. The for screech required five shock cells of the impinging jet are nearly undisturbed from the impinging plate. The shock cell spacing does not differ between the two cases. Only the amplitude of the displacement of the impinging jet profile is slightly decreased. Approaching the impinging plate closer than about

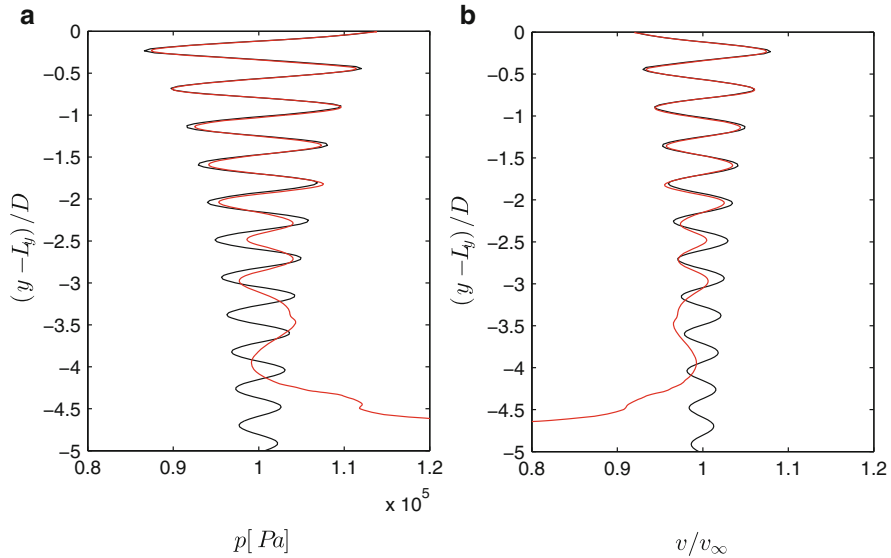


Fig. 12 (a) Pressure and (b) axial velocity profiles along the jet axis of the free *dashed line* and the impinging jet *red solid line* with equal physical parameters

two diameters the impinging jet shock cells are stronger and stronger influenced and disappear. The profiles lead to the conclusion that if screech occurs in the impinging jet noise spectrum it would have to have the exact same frequency as in the free jet case, since the relevant shock cells are even spaced.

Figure 13 shows the noise spectrum of the impinging and the free jet. The impinging jet features a discrete tone at a Strouhal number of $St = 0.353$ accompanied by the first harmonic whereas the free jet tone is at $St = 0.375$ and is missing its harmonics. In order to prove and strengthen the difference of the tones of the two cases, a dynamic mode decomposition using $128 \times 256 \times 128$ points for either simulations was carried out and compared. Figure 14 shows the eigenvalue spectra of the impinging and the free jet. They detect that the screech frequency of the free jet at $St = 0.375$ is a superposition of two frequencies at $St = 0.353$ and $St = 0.399$. On the contrary, the tonal noise of the impinging jet is associated to one mode only. Figure 15 shows the corresponding structures by isosurfaces of the pressure. The impinging jet mode is axis-symmetric however both free jet modes as well as the superposition are helical and even orientated.

The comparison suggests that the tonal noise of the impinging jet is an impinging tone and not associated with screech, since the dominant frequency differs from the one of the free jet despite equal spacings of the relevant shock cells. In addition the corresponding modes have different shapes: single axis-symmetric respectively helical being a superposition of two helical ones (free jet).

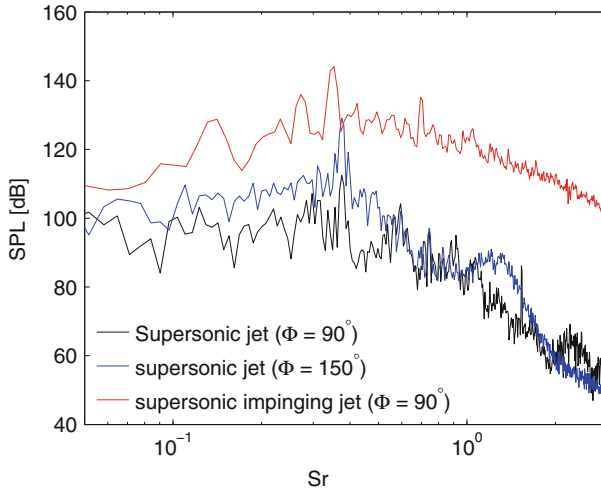


Fig. 13 Noise spectra of the impinging and the free jet. Reference pressure: 2×10^{-5} Pa

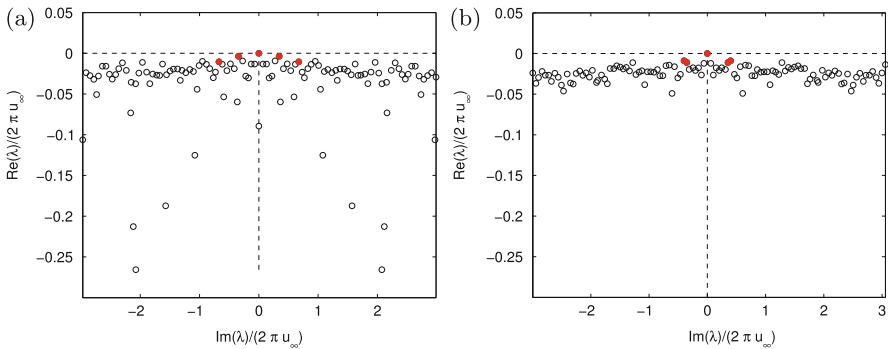


Fig. 14 Eigenvalue spectra of the impinging and free jet, obtained from a DMD. **(a)** Eigenvalue spectrum of the impinging jet, mean value and corresponding frequencies to tonal noise at $Sr = \pm 0.353$ and the first harmonic are marked; **(b)** Eigenvalue spectrum of the free jet, mean value and corresponding frequencies to tonal noise at $Sr = \pm 0.375$ are marked

4.2.2 The Origin of the Impinging Tones

As described before, possible origins of the impinging tones that trigger the feedback mechanism are (a) the primary vortices developing in the shear layer that impinge on the plate and (b) a standoff shock oscillation. Figure 16 shows a sequence representing one period of three dimensional structures of the impinging tone mode ($Sr = 0.353$, without the first harmonic). Vortical structures are detected by Q isosurfaces $Q = 1 \times 10^5 \text{ m}^2 \text{ s}^{-2}$ and coloured green. The standoff shock is detected by isosurfaces of the pressure gradient in y (wall normal) direction $\frac{\partial p}{\partial y} = -2 \times 10^{-5}$ (blue) and $\frac{\partial p}{\partial y} = -2 \times 10^5$ (red). The impinging plate is coloured

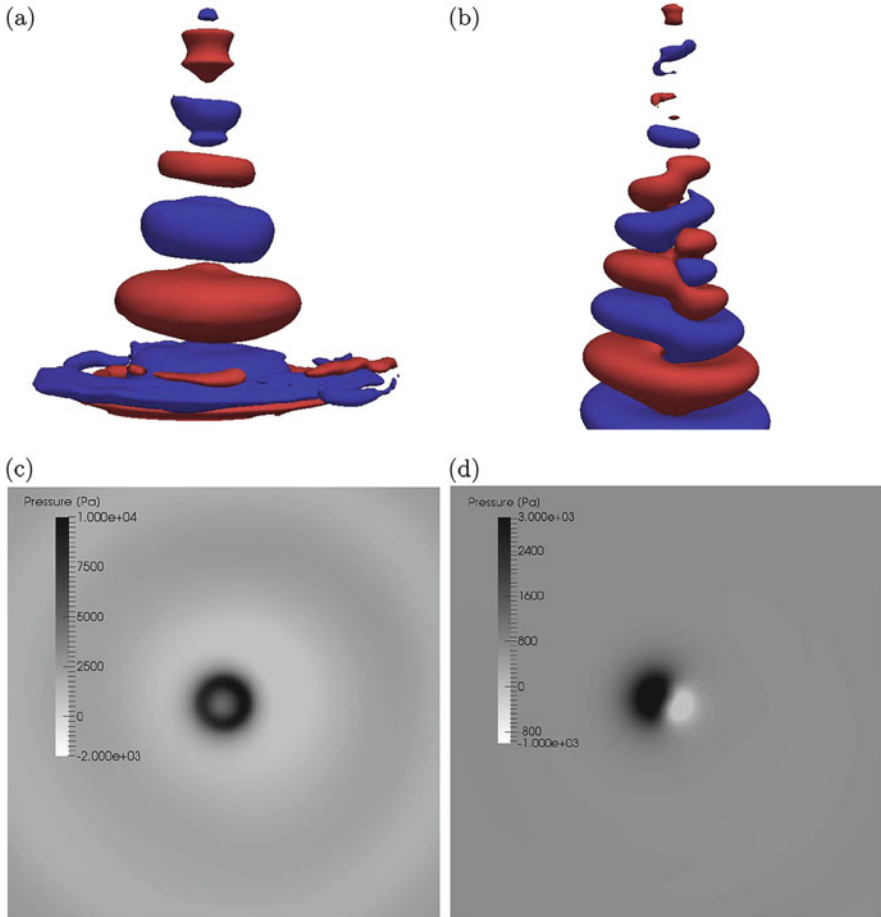


Fig. 15 Dominant dynamic modes of the impinging (a,c) and free jet (b,d) associated with tonal noise. The three dimensional structures are isosurfaces of the pressure (first row). The second row shows the pressure on a cut normal to the jet axis 2 respectively six diameters from the upper plate

with the pressure. It is visible that the impinging tone mode is related to both the primary vortices of the shear layer and the standoff shock oscillation.

The relation between the structures and the acoustic emission can be seen in Fig. 17 that shows snapshots of the flow field at three consecutive time steps (each in one row). The development of the ring vortices in the shear layer as well as the standoff shock can be seen in the first column where Q is depicted. In the final picture (g) the ring vortex reaches the standoff shock. The corresponding velocity divergence is imaged in (i) and shows strong acoustic waves that are radiated and have their origin in the crossing point of the vortex and the shock. This gives evidence that neither the vortices impinging on the plate nor the oscillation itself of the standoff shock is the origin of the impinging tone. The violent interaction

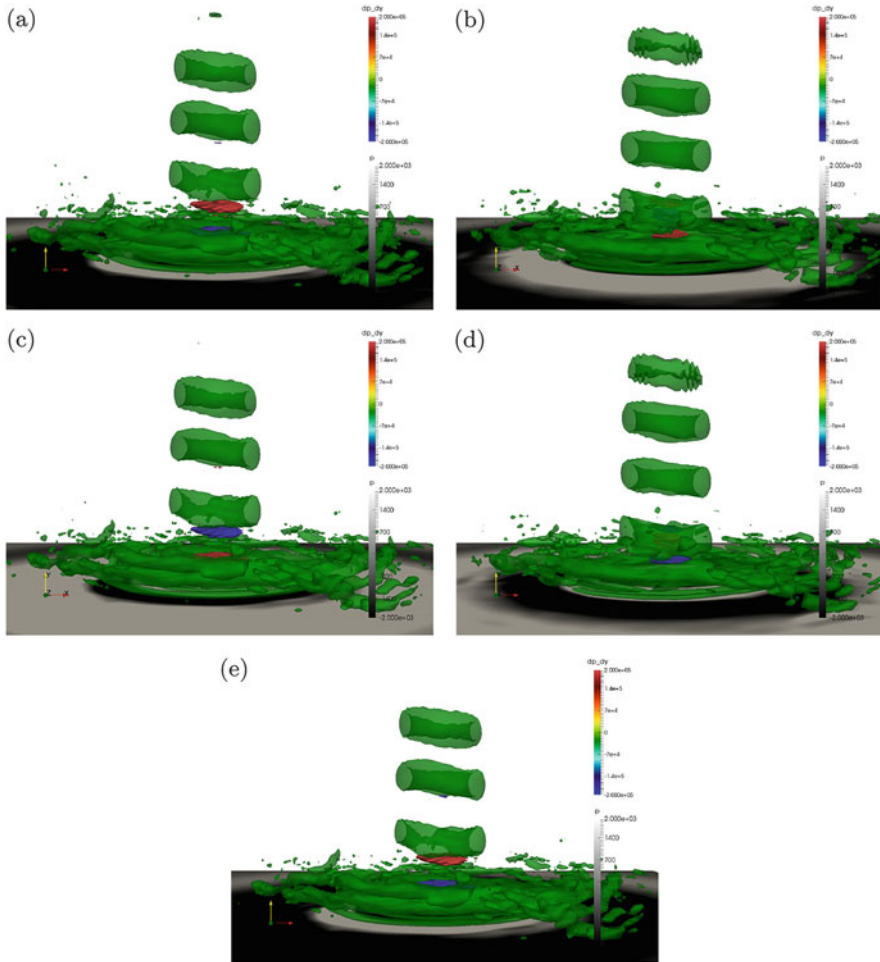


Fig. 16 Dynamic mode of the impinging tone for five equally spaced consecutive time steps (a)–(e) representing one impinging tone cycle. Vortical structures visualised at $Q = 1 \times 10^5 \text{ m}^2 \text{ s}^{-2}$, shock structure visualised at $\frac{\partial p}{\partial y} = \pm 2 \times 10^5 \text{ Pa m}^{-1}$, impinging plate coloured with the pressure

between both players leads to those strong acoustic emissions referred to as impinging tones.

4.3 Conclusion

A DNS of an under-expanded impinging jet at $Re = 3300$, $NPR = 2.15$, $h/D = 5$ was performed using a grid of 512^3 points. The noise spectrum features a discrete tone at $Sr = 0.353$ and its first harmonic. A comparison to a free jet with equal

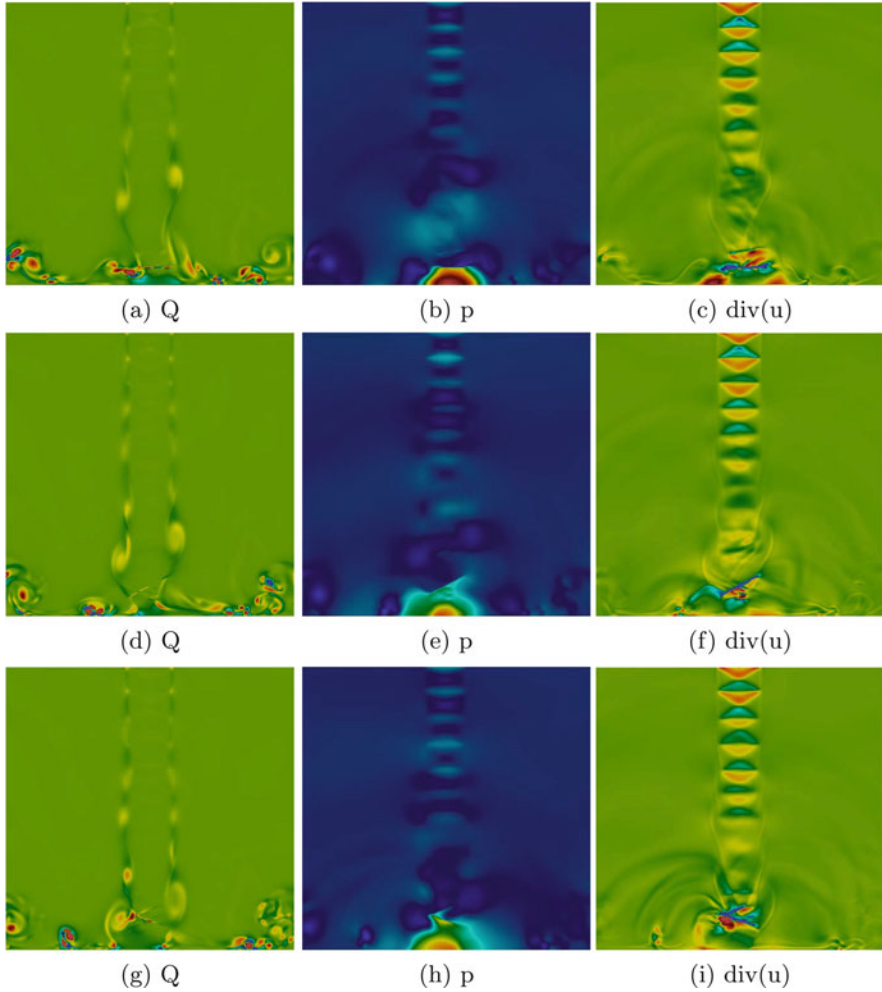


Fig. 17 Snapshots of the flow field at three consecutive time steps (each in one row) showing the interaction between ring vortices and the standoff shock. *First column: Q , second column: pressure and third column: divergence of the velocity*

physical parameters distinguished the tonal noise from screech. The missing chain link in the feedback mechanism of the impinging tones was identified as being the primary vortex-standoff shock-interaction.

Acknowledgements The simulations were performed on the national supercomputer Cray XE6 (Hermit) and Cray XC40 (Hornet) at the High Performance Computing Center Stuttgart (HLRS) under the grant numbers GCS-NOIJ/12993 and GCS-ARSI/44027.

The authors gratefully acknowledge support by the Deutsche Forschungsgemeinschaft (DFG) as part of collaborative research center SFB 1029 “Substantial efficiency increase in gas turbines through direct use of coupled unsteady combustion and flow dynamics”.

References

1. Adams, N.A., Shariff, K.: A high-resolution hybrid compact-ENO scheme for shock-turbulence interaction problems. *J. Comput. Phys.* **127**, S.27–S.51 (1996). <http://dx.doi.org/10.1006/jcph.1996.0156>. doi:10.1006/jcph.1996.0156
2. Bogey, C., de Cacqueray, N., Bailly, C.: A shock-capturing methodology based on adaptive spatial filtering for high-order non-linear computations. *J. Comput. Phys.* **228**(5), 1447–1465 (2009). <http://dx.doi.org/http://dx.doi.org/10.1016/j.jcp.2008.10.042>. doi:http://dx.doi.org/10.1016/j.jcp.2008.10.042. ISSN 0021–9991
3. Buchlin, J.: Convective heat transfer in impinging-gas-jet arrangements. *J. Appl. Fluid Mech.* **4**(3), 137–149 (2011)
4. Chung, Y.M., Luo, K.H.: Unsteady heat transfer analysis of an impinging jet. *J. Heat Transf.* **124**(6), 1039–1048 (2002). <http://dx.doi.org/10.1115/1.1469522>. ISBN 0022–1481
5. Czesla, T., Biswas, G., Chattopadhyay, H., Mitra, N.: Large-eddy simulation of flow and heat transfer in an impinging slot jet. *Int. J. Heat Fluid Flow* **22**(5), 500–508 (2001). [http://dx.doi.org/http://dx.doi.org/10.1016/S0142-727X\(01\)00105-9](http://dx.doi.org/http://dx.doi.org/10.1016/S0142-727X(01)00105-9). doi:http://dx.doi.org/10.1016/S0142-727X(01)00105-9. ISSN 0142–727X
6. Dairay, T., Fortuné, V., Lamballais, E., Brizzi, L.-E.: Direct numerical simulation of a turbulent jet impinging on a heated wall. *J. Fluid Mech.* **764**, 362–394 (2015). <http://dx.doi.org/10.1017/jfm.2014.715>. doi:10.1017/jfm.2014.715. ISSN 1469–7645
7. Eidson, T.M., Erlebacher, G.: Implementation of a fully balanced periodic tridiagonal solver on a parallel distributed memory architecture. *Concurrency Pract. Experience* **7**(4), S.273–S.302 (1995)
8. Hattori, H., Nagano, Y.: Direct numerical simulation of turbulent heat transfer in plane impinging jet. *Int. J. Heat Fluid Flow* **25**(5), 749–758 (2004) <http://dx.doi.org/http://dx.doi.org/10.1016/j.ijheatfluidflow.2004.05.004>. doi:http://dx.doi.org/10.1016/j.ijheatfluidflow.2004.05.004. ISSN 0142–727X. Selected papers from the 4th International Symposium on Turbulence Heat and Mass Transfer
9. Henderson, B.: The connection between sound production and jet structure of the supersonic impinging jet. *J. Acoust. Soc. Am.* **111**(2), S.735–S.747 (2002). <http://dx.doi.org/http://dx.doi.org/10.1121/1.1436069>. doi:http://dx.doi.org/10.1121/1.1436069
10. Henderson, B., Powell, A.: Experiments concerning tones produced by an axisymmetric choked jet impinging on flat plates. *J. Sound Vib.* **168**(2), S.307–S.326 (1993). <http://dx.doi.org/http://dx.doi.org/10.1006/jsvi.1993.1375>. doi:http://dx.doi.org/10.1006/jsvi.1993.1375. ISSN 0022–460X
11. Ho, C.-M., Nossier, N.S.: Dynamics of an impinging jet. Part 1. The feedback phenomenon. *J. Fluid Mech.* **105**(4), S.119–S.142 (1981). <http://dx.doi.org/10.1017/S0022112081003133>. doi:10.1017/S0022112081003133. ISSN 1469–7645
12. Hrycak, P.: Heat Transfer from Impinging Jets. A Literature Review. New Jersey Institute of Technology, Newark, NJ (1981). Forschungsbericht
13. Jambunathan, K., Lai, E., Moss, M., Button, B.: A review of heat transfer data for single circular jet impingement. *Int. J. Heat Fluid Flow* **13**(2), S.106–S.115 (1992). [http://dx.doi.org/http://dx.doi.org/10.1016/0142-727X\(92\)90017-4](http://dx.doi.org/http://dx.doi.org/10.1016/0142-727X(92)90017-4). doi:http://dx.doi.org/10.1016/0142-727X(92)90017-4
14. Janetzke, T.: Experimentelle Untersuchungen zur Effizienzsteigerung von Prallkühlkonfigurationen durch dynamische Ringwirbel hoher Amplitude, TU Berlin, Dissertation (2010)

15. Jungho Lee, S.-J.L.: Stagnation region heat transfer of a turbulent axisymmetric jet impingement. *Exp. Heat Transfer* **12**(2), 137–156 (1999). <http://dx.doi.org/10.1080/089161599269753>. doi:10.1080/089161599269753
16. Lele, S.K.: Compact finite difference schemes with spectral-like resolution. *J. Comput. Phys.* **103**(1), 16–42 (1992). [http://dx.doi.org/10.1016/0021-9991\(92\)90324-R](http://dx.doi.org/10.1016/0021-9991(92)90324-R). doi:10.1016/0021-9991(92)90324-R
17. Panda, J.: Shock oscillation in underexpanded screeching jets. *J. Fluid Mech.* **363**, S.173–S.198 (1998). <http://dx.doi.org/10.1017/S0022112098008842>. doi:10.1017/S0022112098008842. ISSN 1469–7645
18. Pirozzoli, S., Bernardini, M., Grasso, F.: Characterization of coherent vortical structures in a supersonic turbulent boundary layer. *J. Fluid Mech.* **613**, 205–231 (2008). <http://dx.doi.org/10.1017/S0022112008003005>. doi:10.1017/S0022112008003005. ISSN 1469–7645
19. Powell, A.: The sound-producing oscillations of round underexpanded jets impinging on normal plates. *J. Acoust. Soc. Am.* **83**, S.515–S.533 (1988)
20. Powell, A., Umeda, Y., Ishii, R.: Observations of the oscillation modes of choked circular jets. *J. Acoust. Soc. Am.* **92**(5), S.2823–S.2836 (1992). <http://dx.doi.org/http://dx.doi.org/10.1121/1.404398>. doi:<http://dx.doi.org/10.1121/1.404398>
21. Schmid, P.J.: Dynamic mode decomposition of numerical and experimental data. *J. Fluid Mech.* **656**, 5–28 (2010). <http://dx.doi.org/10.1017/S0022112010001217>. doi:10.1017/S0022112010001217. ISSN 1469–7645
22. Schmid, P.: Application of the dynamic mode decomposition to experimental data. **50**(4), 1123–1130 (2011). <http://dx.doi.org/10.1007/s00348-010-0911-3>. doi:10.1007/s00348-010-0911-3. ISBN 0723–4864
23. Schmid, P.J., Sesterhenn, J.L.: Dynamic mode decomposition of numerical and experimental data. In: 61st APS meeting of American Physical Society, San Antonio, p. S.208 (2008)
24. Schulze, J.: Adjoint based jet-noise minimization, TU Berlin, Dissertation (2013)
25. Sesterhenn, J.L.: A characteristic-type formulation of the Navier–Stokes equations for high order upwind schemes. *Comput. Fluids* **30**(1), S.37–S.67 (2001)
26. Sinibaldi, G., Lacagnina, G., Marino, L., Romano, G.P.: Aeroacoustics and aerodynamics of impinging supersonic jets: analysis of the screech tones. *Phys. Fluids* (1994–present) **25**(8) (2013). <http://dx.doi.org/http://dx.doi.org/10.1063/1.4819333>. doi:<http://dx.doi.org/10.1063/1.4819333>
27. Tam, C.K.W.: Supersonic jet noise. *Annu. Rev. Fluid Mech.* **27**(1), 17–43 (1995). <http://dx.doi.org/10.1146/annurev.fl.27.010195.000313>. doi:10.1146/annurev.fl.27.010195.000313
28. Uzun, A., Kumar, R., Hussaini, M.Y., Alvi, F.S.: Simulation of tonal noise generation by supersonic impinging jets. *AIAA J.* **51**(7), S.1593–S.1611 (2013). <http://dx.doi.org/10.2514/1.J051839>. doi:10.2514/1.J051839
29. Viskanta, R.: Heat transfer to impinging isothermal gas and flame jets. *Exp. Thermal Fluid Sci.* **6**(2), S.111–S.134 (1993). [http://dx.doi.org/http://dx.doi.org/10.1016/0894-1777\(93\)90022-B](http://dx.doi.org/http://dx.doi.org/10.1016/0894-1777(93)90022-B). doi:[http://dx.doi.org/10.1016/0894-1777\(93\)90022-B](http://dx.doi.org/10.1016/0894-1777(93)90022-B)
30. Weigand, B., Spring, S.: Multiple jet impingement - a review. *Heat Transf. Res.* **42**(2), S.101–S.142 (2011). ISSN 1064–2285
31. Wilke, R., Sesterhenn, J.L.: Direct numerical simulation of heat transfer of a round subsonic impinging jet. In: *Notes on Numerical Fluid Mechanics and Multidisciplinary Design Bd. 127*, pp. S.147–S.159. Springer, Berlin (2014)
32. Wilke, R., Sesterhenn, J.L.: Numerical simulation of impinging jets. In: *High Performance Computing in Science and Engineering '14*, pp. S.275–S.287. Springer, Berlin (2015)
33. Zuckerman, N., Lior, N.: Impingement heat transfer: correlations and numerical modeling. *J. Heat Transf.* **127**(5), 544–552 (2005). <http://dx.doi.org/10.1115/1.1861921>. ISBN 0022–1481